Please cite this article in press as: Kananian et al., A disposable reader-sensor solution for wireless temperature logging, Device (2023), https://doi.org/10.1016/j.device.2023.100183

Device

CellPress
OPEN ACCESS

Article

# A disposable reader-sensor solution for wireless temperature logging

Siavash Kananian,[1,7] Jihun Rho,[1,7] Cheng Chen,[1] Shahab Mirjalili,[2] Alwin Daus,[1] Min-gu Kim,[3,4] Simiao Niu,[5] Eric Pop,[1] H.-S. Philip Wong,[1] Zhenan Bao,[6] Ali Mani,[2] and Ada S.Y. Poon[1,8,*]

[1]Department of Electrical Engineering, Stanford University, Stanford, CA 94305, USA
[2]Department of Mechanical Engineering, Stanford University, Stanford, CA 94305, USA
[3]Department of Electrical and Computer Engineering, Inha University, Incheon 22212, South Korea
[4]Department of Information and Communication Engineering, Inha University, Incheon 22212, South Korea
[5]Department of Biomedical Engineering, Rutgers University, Piscataway, NJ 08854, USA
[6]Department of Chemical Engineering, Stanford University, Stanford, CA 94305, USA
[7]These authors contributed equally
[8]Lead contact
*Correspondence: adapoon@stanford.edu
https://doi.org/10.1016/j.device.2023.100183

**THE BIGGER PICTURE** The applications of passive wireless sensors are expected to continue growing due to their simplicity, which facilitates daily usage. Ideally, a sensor should be capable of measuring non-transient data, a challenge given their minimalistic design. Additionally, an equally minimalistic reader is needed to facilitate everyday applications. In this context, we introduce a reader that operates through self-oscillation, enabling a flexible, sticker-like reader that is compatible with smartphone NFC technology. The potential for this reader to function with any passive sensor would be of interest to the broader device community. The sensor employs an irreversible phase transition to record non-transient data, demonstrated here through the measurement of the temperature abuse history of food. By addressing the challenge of creating a simple reader and sensor with memory functionality, we have taken a significant step forward in the development of passive wireless sensor-reader systems.

## SUMMARY

Wireless passive sensors, being battery-free and simple, are suitable for disposable use across various applications, from tracking food and monitoring the environment to clinical diagnostics. However, their utilization is hampered by the complexity of existing readout techniques and the absence of memory functionality within the sensor. Here, we present a reader technique that can automatically lock to the sensor value wirelessly through inductive coupling, significantly reducing the reader complexity. By integrating a high-frequency audio link and wireless powering, we demonstrate a battery-free and flexible reader. We integrated this reader for wireless temperature logging, which logs temperature data based on the irreversible geometric change of low-melting-point metal during phase transitions, resulting in non-volatile resistance change. As a whole, these results establish the feasibility of a simplistic reader and a passive non-volatile thermistor sensor, opening up new possibilities for disposable and ubiquitous temperature monitoring as well as a range of other applications.

## INTRODUCTION

Wireless passive sensors, known for their battery-free and chipless design (Figure 1A), offer an inexpensive disposable solution for applications ranging from wearables, clinical diagnostics, and food tracking to environmental monitoring. In contrast to colorimetry-based sensors,[1] wireless passive sensors provide additional benefits, such as enhanced security and electronic processability. Significant research efforts have been focused on broadening the range of stimulus modalities to include physical parameters beyond pressure.[2] This includes temperature,[3] dielectric properties of liquid food,[4] and pH levels of packaged meat.[5] Additionally, efforts have been made to enhance the capabilities of these sensors by incorporating features such as memory function,[5,6] biodegradability,[7,8] conformability,[7,9] stretchability,[10] ease of manufacture,[4] and miniaturization.[11] These sensors are typically embedded as part of a resistor-inductor-capacitor (RLC) resonant circuit, where stimuli are


This is an open access article under the CC BY-NC-ND license (http://creativecommons.org/licenses/by-nc-nd/4.0/).

Please cite this article in press as: Kananian et al., A disposable reader-sensor solution for wireless temperature logging, Device (2023), https://doi.org/10.1016/j.device.2023.100183



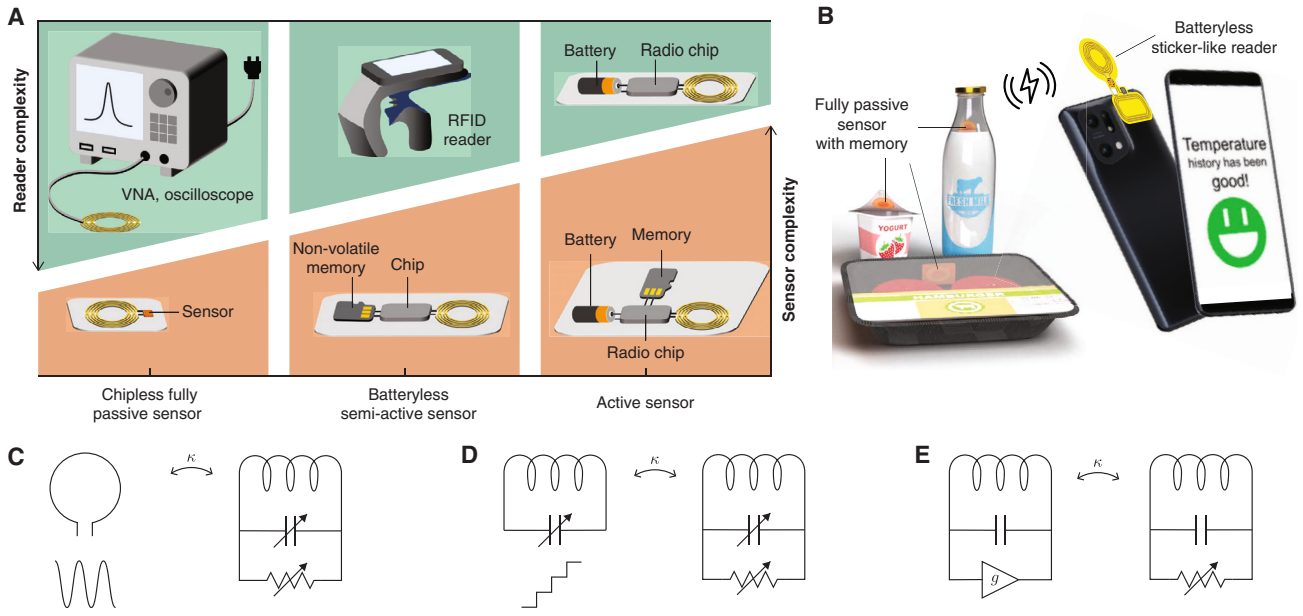


**Figure 1. A comparison of conventional and proposed reader-sensor systems**

(A) Current reader-sensor systems can be collectively classified into three major categories according to the sensor architecture: chipless fully passive (left), battery-less semi-active (center), and active (right) sensors. There is an asymmetry in the complexity of the sensor (bottom) and its corresponding reader (top). Passive sensors do not need a battery and are chipless. They usually consist of a resistor-inductor-capacitor (RLC) resonant circuit. Because the sensor is relatively simple, the reader tends to be complex and bulky, using a vector network analyzer (VNA) or an oscilloscope. Semi-active sensors can perform some processing, with power typically being extracted from an external source. The reader becomes simpler; for example, an RFID (radio-frequency identification) reader. Active sensors consist of an antenna, a standard-compliant radio chip and other electronic circuitry, and a battery. Due to its high complexity, the reader is relatively simple; for example, a standard radio solution.

(B) The proposed reader-sensor system shows matching levels of complexity between the reader and the fully passive sensor. The reader, which operates without a battery, is attached to the back of a smartphone for both power and display purposes, while the sensor is placed in a food package.

(C and D) Conventional passive sensor and reader schemes based on (C) forced excitation and (D) capacitance sweeping at the reader to achieve active tuning.

(E) Schematics of the proposed passive sensor and reader.

converted into resonant frequency shifts and/or amplitude changes. These changes are wirelessly measured by an inductively coupled reader. This reader is actively tuned for robustness against variations in operating conditions and/or to match the frequency shift induced by the stimulus. The active tuning is achieved through either frequency sweeping of a forced excitation source[7–16] (Figure 1C) or capacitance sweeping[15–19] (Figure 1D). While most of the research on reader design focuses on improving the sensitivity of the reader-sensor link, the use of forced excitation and/or closed-loop control for active tuning makes the implementation of the reader complex. The substantial complexity gap between the reader and the sensor (Figure 1A) presents a challenge to the widespread utilization of wireless passive sensors, especially when monitoring perishable goods, where affordable and widely available readers are crucial.

Here, we present a wireless reader design that is battery free and simple, along with a passive non-volatile thermistor sensor (Figure 1B). We model the wireless link as a weakly nonlinear coupled oscillator and theoretically derive the nonlinearity condition for the reader to automatically lock to the sensor value wirelessly through inductive coupling (Figure 1E). This automatic locking approach significantly reduces the complexity of the reader. By integrating a high-frequency audio link and wireless powering, we demonstrate a sticker-like, battery-free reader (Figure 1B) that paves the way for disposable solutions. For the sensor, temperature logging is achieved by the irreversible change in the geometry of low-melting-point metal during solid-liquid phase transitions. As the metal undergoes phase transitions from solid to liquid and vice versa around a critical temperature, its geometry undergoes changes that affect the electrical resistance. This results in a non-volatile resistance change in the RLC resonant circuit that can be interrogated by the self-oscillating reader (Figure 1E).

## RESULTS

### Operation principle of the self-oscillating reader

We present an analysis based on modeling the coupled reader-sensor as a weakly nonlinear oscillator. The reader consists of an inductor-capacitor (LC) circuit and a negative resistor with current-voltage (I-V) characteristics denoted by $\frac{i}{I_0} = g\left(\frac{v}{V_0}\right)$ and is inductively coupled to the sensor resonator (Figure 2A), where $I_0$ and $V_0$ are constants for normalization. At steady state, this coupled system has three eigenfrequencies in the strongly coupled region.[20] These eigenfrequencies are coupling dependent. When the reader and the sensor exhibit matched

Please cite this article in press as: Kananian et al., A disposable reader-sensor solution for wireless temperature logging, Device (2023), https://doi.org/10.1016/j.device.2023.100183



CellPress
OPEN ACCESS

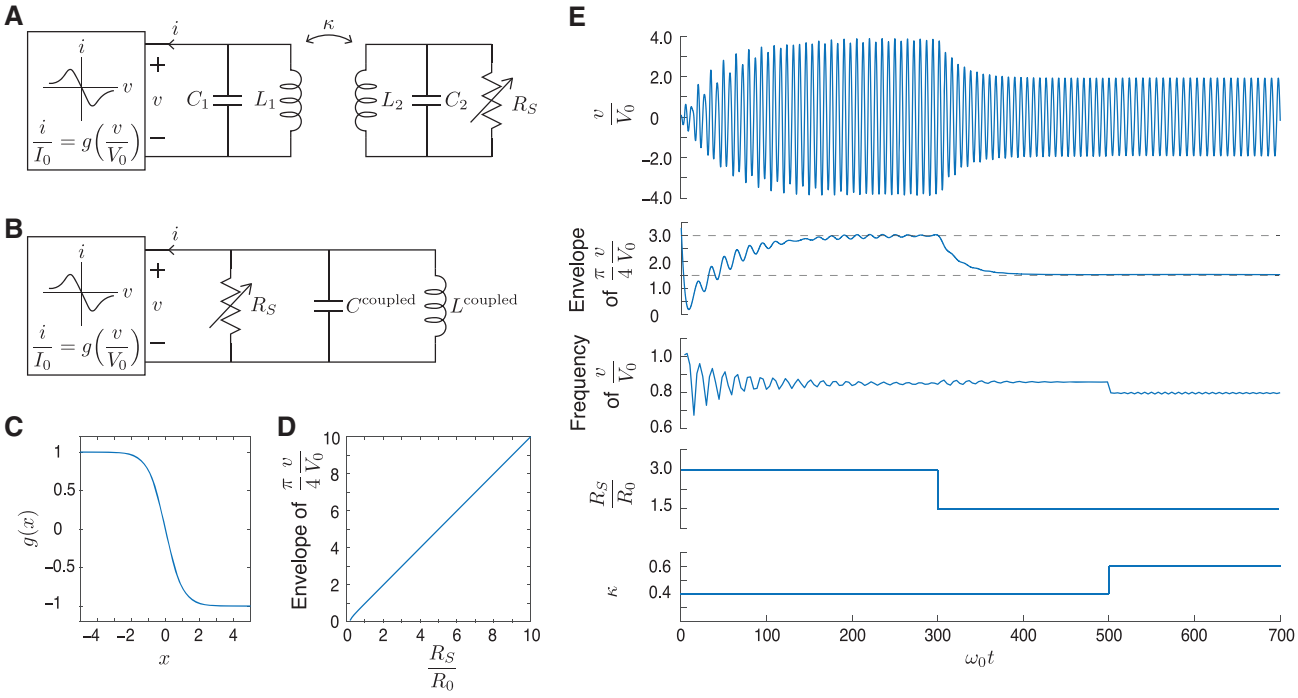


**Figure 2. The self-oscillating reader automatically locks to sensor values**

(A) Schematic of the coupled reader-sensor system.

(B) Equivalent model of the coupled system in a stable mode.

(C) Normalized I-V curve of the negative resistance, $g(x) = -\tanh(5x)$.

(D) Normalized amplitude of the voltage across the negative resistor at steady state, scaled by a factor $\frac{\pi}{4}$ as a function of normalized sensor resistance $\varepsilon = 0.25$..

(E) Simulated transient response of the normalized voltage across the negative resistor (top), its envelope scaled by a factor $\frac{\pi}{4}$ (center top), and its frequency (center). These simulations are based on the coupled reader-sensor system in (A) where $\frac{1}{R_0}\sqrt{\frac{L}{C}}$ is set to 0.25, starting from an initial value of $\frac{v}{V_0} = 0.1$, and then over a sudden change in the normalized sensor resistance from 3 to 1.5 at $\omega_0 t = 300$ (center bottom) and a sudden change in the coupling coefficient from 0.4 to 0.6 at $\omega_0 t = 500$ (bottom). In these simulations, $L_1 = L_2 = L$, $C_1 = C_2 = C$, and $\omega_0 = \frac{1}{\sqrt{LC}}$.

resonance, the impedance seen at the reader over the two stable modes equals the sensor resistance $R_S$, independent of the coupling. This property has been exploited to achieve coupling-independent wireless power transfer[21,22] and wireless sensing.[20] Here, we utilize this property to theoretically and experimentally demonstrate a simple reader for wireless passive resistive sensors.

For each stable mode, the fourth-order coupled system shown in Figure 2A can be transformed into a second-order system as shown in Figure 2B (experimental procedures). The system dynamics are described by

$$\ddot{x} + x + \varepsilon\left[\frac{R_0}{R_S} + g'(x)\right]\dot{x} = 0 \qquad \text{(Equation 1)}$$

where $x = \frac{v}{V_0}, R_0 = \frac{V_0}{I_0}, \varepsilon = \frac{1}{R_0}\sqrt{\frac{L^{\text{coupled}}}{C^{\text{coupled}}}}$, and the time derivative is taken w.r.t. $\omega_0^{\text{coupled}} t$ and $\omega_0^{\text{coupled}} = \frac{1}{\sqrt{L^{\text{coupled}} C^{\text{coupled}}}}$. When $\frac{\pi}{4}$ is small, it is a weakly nonlinear oscillator.[23] We can apply the method of multiple scales to separate processes occurring at different time scales. In this case, the fast time is $\tau = \omega_0^{\text{coupled}} t$, and the slow time is $T = \varepsilon\tau$. The solution to Equation 1 can be expanded as follows:[23]

$$x(\tau) = x_0(\tau, T) + \varepsilon x_1(\tau, T) + O(\varepsilon^2). \qquad \text{(Equation 2)}$$

Substituting into Equation 1 and collecting powers of $\varepsilon$ yield the general solution to $x_0$:

$$x_0(\tau, T) = r(T)\cos(\tau + \varphi(T)), \qquad \text{(Equation 3)}$$

which is a simple harmonic oscillator with slowly varying amplitude $r(T)$ and phase $\varphi(T)$. By the method of averaging,[23] we obtain

$$r' = -\frac{R_0}{R_S} - \frac{1}{2\pi}\int_0^{2\pi} g(r\cos\theta)\cos\theta d\theta. \qquad \text{(Equation 4)}$$

Our goal is to find $g(\cdot)$ so that Equation 1 models an oscillator and $r' = 0$ has a stable fixed point that is proportional to $R_S$. One such solution is a step function: $g(x) = -1$ when $x \geq 0$ and $g(x) = 1$ when $x < 0$. The stable fixed point is $r^* = \frac{4}{\pi}\frac{R_S}{R_0}$, and the radius of the limit cycle is $\frac{4}{\pi}\frac{R_S}{R_0} + O(\varepsilon)$, asymptotically proportional to the sensor resistance.

To evaluate the asymptotic result, we approximate the step function by a sigmoid function (Figure 2C). The amplitude of the normalized voltage across the negative resistor at steady

Please cite this article in press as: Kananian et al., A disposable reader-sensor solution for wireless temperature logging, Device (2023), https://doi.org/10.1016/j.device.2023.100183



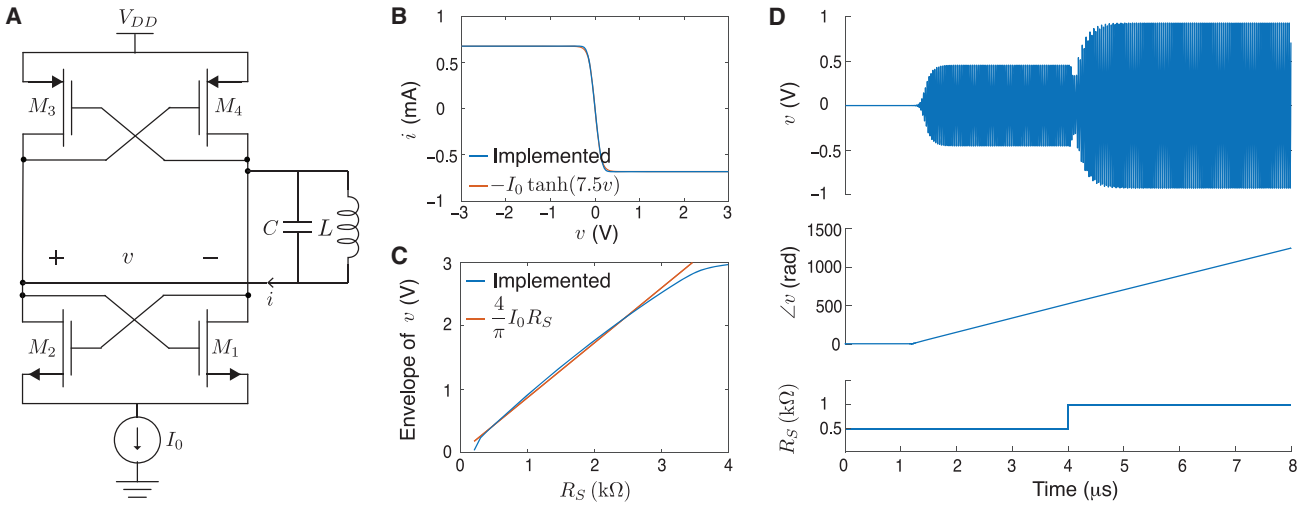


**Figure 3. Realization of the self-oscillating reader**

(A) Circuit diagram of the negative resistance oscillator.

(B) I-V curve of the negative resistor, showing the nonlinearity profile of the negative resistance that follows the function $i = -I_0 \tanh(7.5v)$.

(C) Amplitude of the voltage across the negative resistor at steady state as a function of sensor resistance, showing good agreement with the calculated value to demonstrate the operational range of the sensor.

(D) Simulated transient response of the voltage across the negative resistor (top) and its phase (center) for a coupled reader-sensor system with $\kappa = 0.4$ from an initial value of 10 mV and then over a sudden change in Rs from 500 Ω to 1 kΩ at 4 μs (bottom), showing the automatic locking capability of the reader and confirming the weakly nonlinear assumption of the coupled system.

state scales linearly with the normalized sensor resistance at a slope of $\frac{4}{\pi}$ (Figure 2D). To evaluate the automatic locking capability of the self-oscillating reader, we solve the fourth-order non-linear dynamic system in Figure 2A. Starting with a small initial value, the reader takes about 25 cycles to lock to the sensor value and about 10 cycles for a sudden 50% change in the sensor resistance (Figure 2E). At steady state, the envelope of the normalized voltage when scaled by a factor of $\frac{\pi}{4}$ tracks the normalized sensor resistance very closely. The envelope remains locked to the sensor value even when there is a sudden change in the coupling between the reader and the sensor, during which the frequency of the coupled oscillator is automatically adjusted.

## Integrated circuit implementation of the reader

Building upon this theoretical framework from the previous section, we have developed a device to experimentally validate the theory and assess its practical functionality. Among various realizations of negative resistance, the I-V characteristics of a cross-coupled transistor pair can be designed to be close to the desired step function.[24] Bipolar junction transistors have a steeper I-V relationship during transition than that of metal-oxide-semiconductor field-effect transistors (MOSFETs); however, MOSFETS are much better for integration. Among MOSFET-based topologies, the multiplicative factor $\frac{4}{\pi R_0}$ achieved by a complementary metal-oxide semiconductor (CMOS) is twice as that by an N-channel metal-oxide semiconductor (NMOS). We therefore demonstrate the theoretical result presented above by realizing the desired step function by a cross-coupled CMOS pair (Figure 3A; Table S1). Figure 3B shows the simulated I-V curve of our implemented negative resistor and its approximation by $i = -I_0 \tanh(7.5v)$. The amplitude of the voltage across the negative resistor at steady state scales linearly with the sensor resistance at a slope of $\frac{4}{\pi} I_0$ when $R_S < 3$ kΩ (Figure 3C). At higher values of $R_S$, the swings get larger, and, thus, the current source implemented using an NMOS transistor goes into the triode region and results in its current no longer being equal to $I_0$. To evaluate the automatic locking capability, the reader circuit is coupled to a sensor resonator. Starting with a small initial value, the reader takes about 1.5$\mu$ s to lock to the sensor value and about 0.5$\mu$s for a sudden 50 % change in sensor resistance (Figure 3D). After initialization, the phase of the voltage scales linearly with time, confirming the weakly nonlinear assumption. Details about the stimulation are provided under experimental procedures.

The simplicity of the self-oscillating reader leads to its implementation in a custom application-specific integrated circuit (ASIC) occupying a die area of 1 mm$^2$ and consuming 2.2 mW of power[25] (Figure 4A; experimental procedures). The low power consumption supports battery-free operation through power harvesting from the polling mode of near-field communication (NFC) on a smartphone without the need of an NFC chip in the reader[25] (Figure 4B; experimental procedures). For increased versatility and simplicity, we use an audio link for information transmission to be exempt from compliance with any wireless communication standard. Any device with a microphone can be securely programmed as a receiver. The on-chip audio transmitter is implemented in the frequency range of 16–20 kHz[25] because the hearing threshold is much higher compared with lower frequencies.[26] The sensor value is locked by the cross-coupled CMOS pair and envelope detector (Figure 4C). The output of the envelope detector is frequency modulated, and

Please cite this article in press as: Kananian et al., A disposable reader-sensor solution for wireless temperature logging, Device (2023), https://doi.org/10.1016/j.device.2023.100183



CellPress
OPEN ACCESS

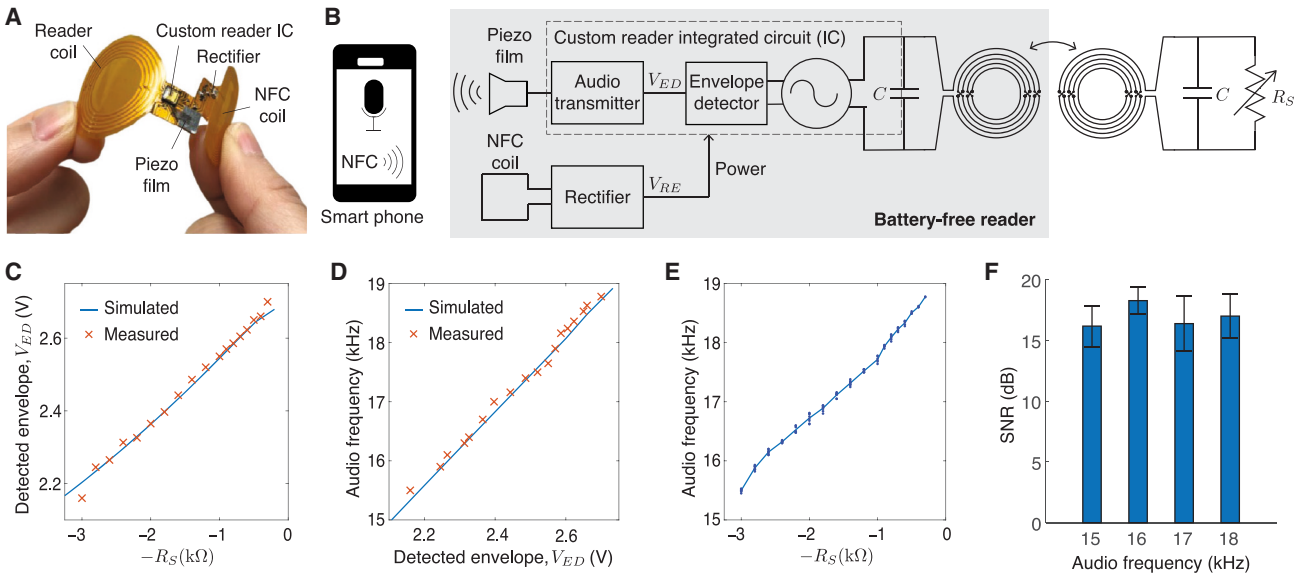


**Figure 4. Implementation of a battery-free, sticker-like reader**

(A) Photograph of the reader showing all circuit components, demonstrating its flexible form factor.

(B) Conceptual diagram showing the design and operation of the reader.

(C) Detected envelope of the normalized voltage versus sensor resistance, demonstrating that the sensor resistance value is translated into the voltage of the oscillator and the measured results matching the simulation results.

(D) Audio frequency recorded on the smartphone versus detected envelope, showing the successful translation of the oscillator through the audio link and measured results matching simulation results.

(E) Audio frequency recorded on the smartphone versus sensor resistance, demonstrating an almost linear dependence.

(F) Signal-to-noise ratio of the audio link for transmission distance varying between 2 and 4 cm, demonstrating reliable performance within the provided range.

the modulated signal is transmitted via a piezoelectric thin film (Figure 4D) with a sound pressure level (SPL) of less than 30 decibels (dB; measured right at the piezoelectric thin film), which is practically inaudible for humans. Figure 4E demonstrates the overall performance of the audio transmitter, confirming that the measured audio frequency is approximately proportional to the sensor value. The power consumption of the audio transmitter is 54 μW, about two orders of magnitude less than any low-power wireless standard. Figure 4F shows the signal-to-noise ratio of the audio link for a transmission distance varying between 2 and 4 cm. The average link signal-to-noise ratio is above 15 dB, which is substantially above the requirement for reliable transmission. During operation, the reader is attached to the back of a smartphone for power and display (Figure 1D). Details about the characterization setup for the reader-sensor link are provided under experimental procedures. Overall, this demonstrates the feasibility of a battery-free, sticker-like reader for passive resistive sensors.

## Wireless passive non-volatile thermistor sensor

Previous studies have investigated irreversible impedance changes of pH-sensitive coatings and dielectric changes of polymers to develop wireless passive pH and chemical sensors with memory functions.[5,6] In this work, we leverage the irreversible change in the geometry of low-melting-point metals to enable memory functionality in a wireless passive temperature sensor. Low-melting-point metals are highly conductive and available in various alloys with different melting points. During the solid-liquid phase transition, the structure of a low-melting-point metal deforms, which can be utilized to implement a non-volatile binary thermistor sensor. A system of $N$ binary sensors made from alloys of different melting points ($T_n$s) form a wireless, passive, non-volatile thermistor sensor (Figures 5A and S1). For simplicity, but without loss of generality, we demonstrate this idea for $N = 1$ with gallium-based low-melting-point metals.

The structure of the solid gallium before melting has an inverted U shape, with its top part forming an electrical connection with two separate carbon electrodes (Figure S2). When it is exposed to a temperature higher than its melting point, the structure starts to deform from the side. After the phase transition is completed, the entire gallium structure shrinks due to its high surface tension, forming an open gap ($\Delta$) with the carbon electrode (the high-impedance state), as illustrated in Figure 5B. This melting trajectory has been validated through both simulation and experimentation (Figure 5B; experimental procedures; Videos S1 and S2). When the circuit has transitioned into the high-impedance state, it remains in that state even when the temperature decreases below the melting point. This persistence of high impedance occurs because of the irreversible nature of the deformation process. To summarize, the output resistance value from the sensor retains non-transient information about the environment, effectively functioning as a memory that conveys binary data, indicating whether the sensor has been exposed to temperatures higher than the melting point of gallium.

Please cite this article in press as: Kananian et al., A disposable reader-sensor solution for wireless temperature logging, Device (2023), https://doi.org/10.1016/j.device.2023.100183



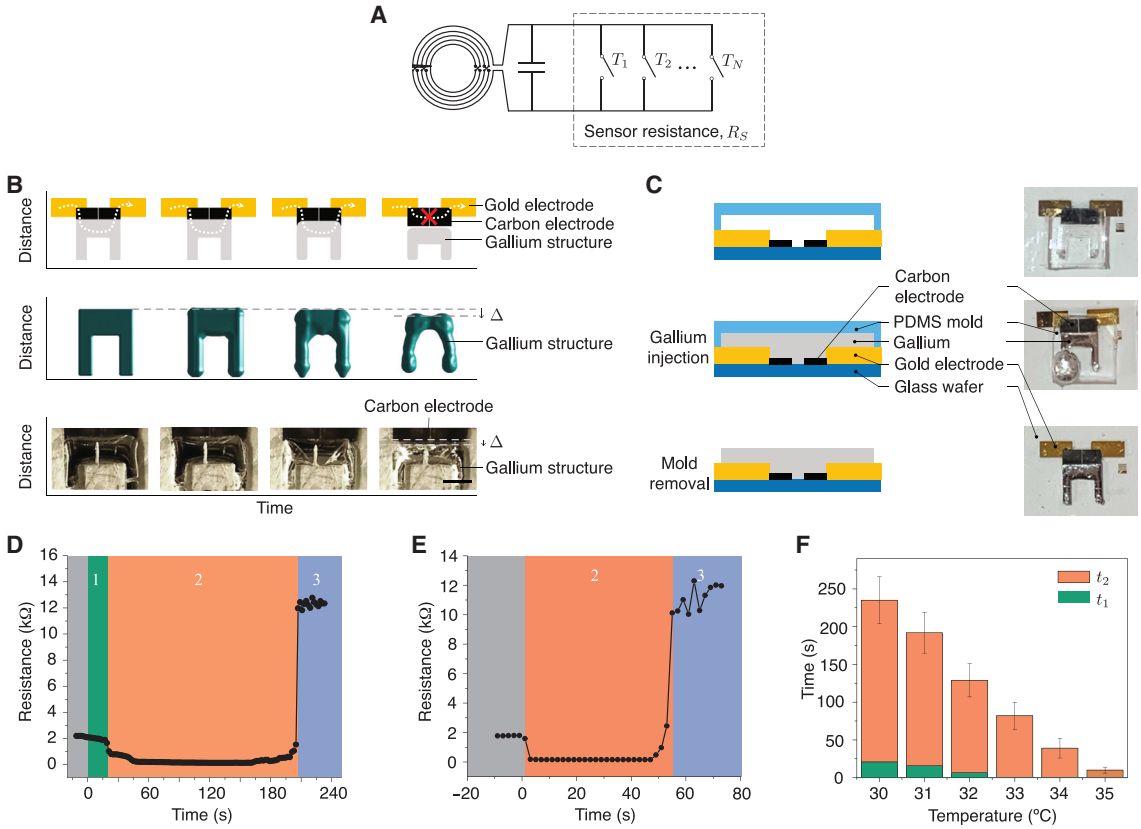


**Figure 5. Concept, realization, and characterization of the passive non-volatile thermistor sensor**

(A) Conceptual diagram showing the design of a non-volatile thermistor sensor forming from a system of binary sensors.

(B) Illustration of the current flow (dotted line) in the gallium structure (top), simulation of the deformation of an inverted U-shaped gallium structure at an exposed temperature of 32°C, and the corresponding experimental result (bottom). Scale bar: 2 mm.

(C) Fabrication process for the sensor. The PDMS mold on the carbon electrode is filled with liquid gallium to be solidified.

(D and E) Transient responses of the sensor resistance for a sample exposed to (D) 31°C and (E) 34°C. This demonstrates how the sensor's resistance changes over time during exposure to heat.

(F) Delay in heat transfer ($t_1$) and switching time ($t_2$) of the sensor as a function of the exposed temperature, illustrating the sensor's temperature-dependent behavior for response time.

Figure 5C summaries the fabrication process for the binary sensor (melting point at 29.8°C;[27] experimental procedures). Figure 5D shows the transient response of the sensor resistance for a sample exposed to 31°C (experimental procedures). Collectively, the transition can be partitioned into 3 stages. In the first stage, the region shaded in green and marked as 1, the resistance stays the same as before phase transition. Heat is transferred into the substrate, leading to the melting of gallium starting from the surface of the structure (stage 2, shaded in orange). Gallium is known to exhibit an increase in conductivity after melting, which we believe is the primary reason for the observed decrease in resistance in stage 2.[28] In the third stage (the region shaded in blue, marked as 3), the gallium structure is completely melted, forming a gap with the carbon electrode, resulting in a high-impedance state. Time spent in the first stage ($t_1$) reflects the delay in the heat transfer and diminishes with increasing temperature (Figure 5E). Time spent in the second stage ($t_2$) also depends on the exposure temperature (Figure 5F). As the exposure temperature increases, the total switching time, including the delay ($t_1$ + $t_2$), decreases from 235 s at 30°C to 10.5 s at 35°C.

We investigated the potential impact of humidity on the sensor's performance. It is well documented that the viscosity of gallium increases with higher humidity levels.[29] However, with the current sensor design, which strongly relies on the solid-to-liquid phase transition, humidity appears to exert minimal to negligible influence on the sensor's behavior (Figure S3A). While it is recognized that carbon nanotubes (CNTs) exhibit increased resistivity in response to rising humidity,[30] our sensor also demonstrated this effect. Nonetheless, the observed increase was relatively small, approximately 10 Ω with a 10% increase in relative humidity, and did not significantly affect the sensor's performance, as shown in Figure S3B.

## Demonstration of wireless temperature logging

Finally, we demonstrate tracking of temperature-sensitive chocolate truffles using the self-oscillating reader and the passive temperature sensor. We first validate the wireless reader-sensor

Please cite this article in press as: Kananian et al., A disposable reader-sensor solution for wireless temperature logging, Device (2023), https://doi.org/10.1016/j.device.2023.100183



CellPress
OPEN ACCESS

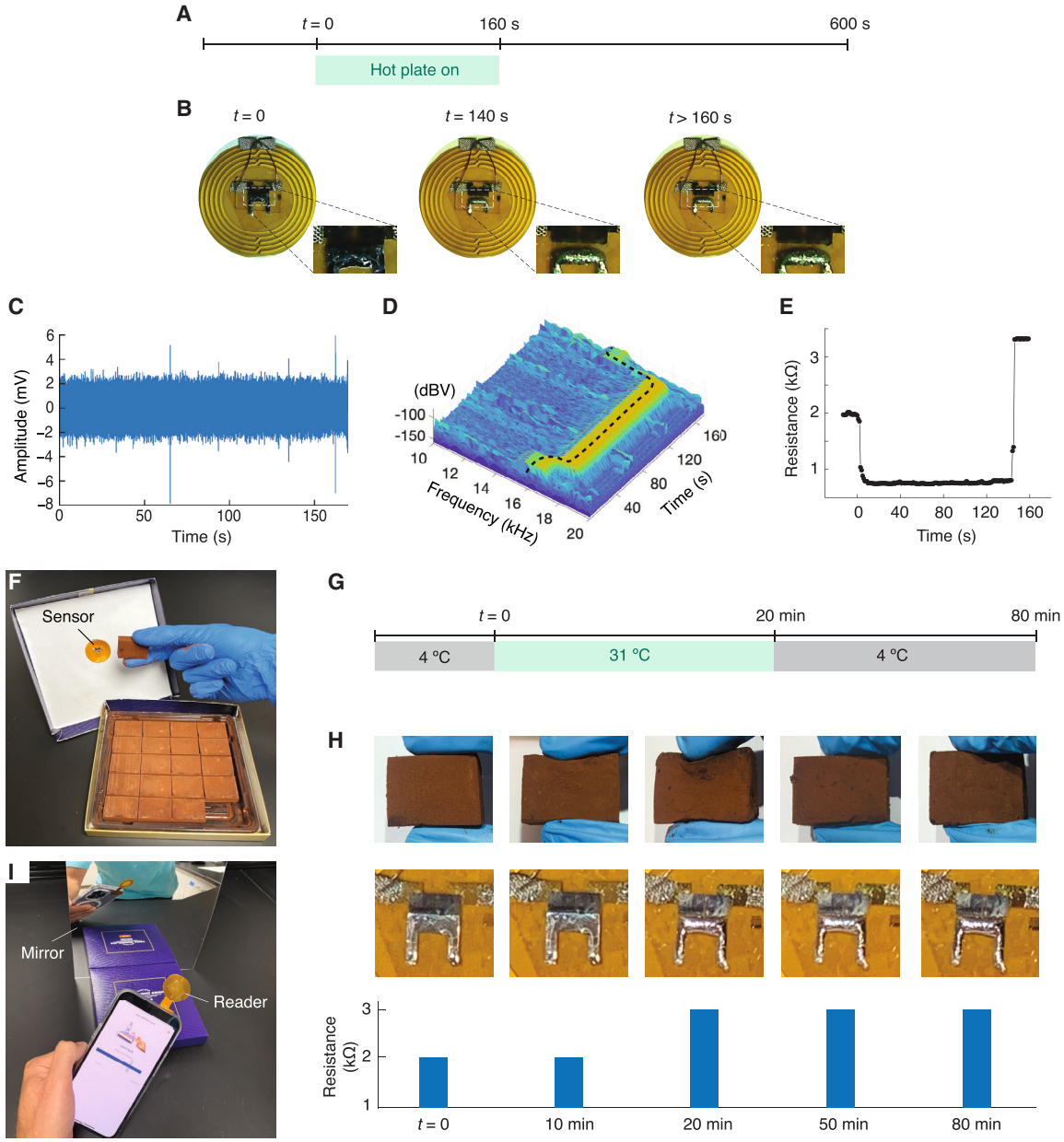


**Figure 6. Detection of temperature abuse in temperature-sensitive products**

(A) Experimental procedure for applying heat to the sensor.

(B) Photographs of the sensor at different times, showing its state.

(C) Amplitude of recorded audio signals on the phone when the hot plate is on.

(D) Spectrogram of the measured frequency of the audio signal, which depends on the sensor resistance, showing three distinct stages of the sensor during heat exposure.

(E) Resistance value converted from (D).

(F) Photograph of a passive irreversible temperature sensor placed in a food package and concealed from the outside.

(G) Timeline for the concealed detection experiment.

(H) Photographs showing the texture of chocolate truffles (top), photographs showing the state of the sensor (center), and measured resistance from the reader at different times (bottom). This demonstrates that the temperature abuse event that occurred within the first 20 min is measurable at any time following the event.

(I) Photograph of the reader (attached to the back of a smartphone as seen from the mirror image) interrogating the sensor resistance in which the state of the sensor is displayed on the phone (see also Figure S6).

Please cite this article in press as: Kananian et al., A disposable reader-sensor solution for wireless temperature logging, Device (2023), https://doi.org/10.1016/j.device.2023.100183



link by heating the wireless temperature sensor directly on a hot plate (26°C–32°C) for 160 s (Figure 6A; experimental procedures). During heat exposure, the sensor changes from the low-impedance state to the high-impedance state. Even after the heat source is removed, the sensor remains in the high-impedance state, verifying its irreversibility (Figure 6B). Figure 6C plots the audio signal recorded on the phone during heat exposure. Its Fourier transform confirmed the three distinct stages (Figures 6D and 6E). The wireless sensor is then attached to the inside of a box of temperature-sensitive chocolate truffles (Figure 6F). Simulating a scenario where the box is exposed at room temperature on a hot day for a short period of time (Figure 6G; experimental procedures), Figure 6H shows the change in the texture of the chocolate, the state of the sensor, and the resistance measured by the reader. After 20 min at 31°C, the chocolate became softer and the sensor switched states. Subsequent refrigeration hardened the chocolate. It is imperceptible by naked eye that the chocolate has melted and solidified again. However, this can be uncovered by the reader from the outside while the package is intact (Figure 6I; Video S3).

## DISCUSSION

Here we present a theoretical study of a self-oscillating reader capable of automatically locking to the sensor value and show that this property can be used to dramatically reduce the complexity of wireless readers. By integrating a high-frequency-audio wireless link and wireless powering, we demonstrate the feasibility of a sticker-like and battery-free reader, which brings simplicity to a level comparable with that of wireless passive sensors. Reducing the complexity gap is pivotal to unlock the potential of wireless passive sensors in everyday applications. Envisioning a scenario where these readers are readily available in grocery stores, we could easily attach one to our phone. With this setup, we could effortlessly retrieve the history of perishable foods, empowering us as a consumer.

In the self-oscillating reader, the fully passive sensor becomes part of the LC resonant circuit of the reader, which, together with the negative resistance, forms an LC oscillator. The nonlinear negative resistance allows autonomous settling of the oscillation amplitude to a value proportional to the RLC sensor's resistance. If the reader and sensor LC resonant tanks have equal resonant frequencies, then the amplitude of oscillation remains independent of the coupling strength between the two, allowing distance-independent measurement of the passive sensor. The distance must remain within a certain critical coupling range, mainly determined by the dimensions of the coils and the sensor value.[25] If the distance between the two changes, the autonomous behavior of the coupled resonators adjusts the frequency of oscillation so that the amplitude remains constant. Similarly, in response to a change in the sensor value, the amplitude of oscillation will change proportionally. This self-oscillating reader eliminates the need for forced excitation in existing solutions for measurement for fully passive sensors. The reader employs an audio signal uplink that is well-suited for low-power solutions due to the order of magnitudes lower frequency of operation. Given that the sensor measurements are converted to a change in the frequency of the audio signal tone, the resulting signal is narrow band and can be transmitted well within the operation frequency of audio consumer products, such as a cellphone microphone.

In addition, we extend the utility of wireless passive temperature sensors to include memory functions. The proposed sensor utilizes the change in the physical structure of gallium induced by the temperature-induced phase change. When gallium melts, its structure undergoes an irreversible change as it attempts to minimize the surface area of the liquid. This phenomenon has been verified through both experimental and simulation approaches. The structure was fabricated using classic soft lithography, employing polydimethylsiloxane (PDMS) as a mold. This fabrication method allows easy manipulation of the physical specifications, such as the size, shape, and thickness of the structure. Consequently, different time and temperature conditions can be applied to induce the phase transition due to the distinct heat transfer characteristics of the structure.[31] The gallium's structural transformation initiates a transition in the current path, progressing from low resistance to high resistance. This ultimately leads to a high resistance value detected by the wireless reader.

In future work, the operational temperature range of this sensor could be easily modified by using established low-melting gallium alloys and alkali-metal alloys.[32] Moreover, the design of a multilevel non-volatile sensor could be readily achieved by incorporating multiple binary sensors, each with substrates possessing varying thermal conductivities. Apart from addressing last-mile food safety, the proposed disposable reader and sensor solution has the potential to be applied to various emerging applications that require extensive deployment, such as structural monitoring and health monitoring. This represents a significant advancement in the realm of maintenance-free and ubiquitous monitoring, signifying a paradigm shift in the field.

## EXPERIMENTAL PROCEDURES

### Resource availability

#### *Lead contact*

Further information and requests for resources should be directed to and will be fulfilled by the lead contact, Ada S.Y. Poon (adapoon@stanford.edu).

#### *Materials availability*

This study did not generate new unique reagents.

#### *Data and code availability*

All data and code generated during the study are available from the lead contact upon reasonable request.

### Modeling the coupled reader-sensor system as a second-order system in each stable mode

Referring to the coupled system in Figure 2A and assuming solutions with harmonic time dependence $e^{j\omega t}$, we denote the complex voltage across inductor $L_n$ by $V_n$ and the complex current through it by $I_{Ln}$ for $n = 1, 2$. These voltages and currents are related by

$$\begin{bmatrix} V_1 \\ V_2 \end{bmatrix} = j\omega \begin{bmatrix} L_1 & \kappa\sqrt{L_1 L_2} \\ \kappa\sqrt{L_1 L_2} & L_2 \end{bmatrix} \begin{bmatrix} I_{L1} \\ I_{L2} \end{bmatrix}. \quad \text{(Equation 5)}$$

Applying Kirchoff's current law yields

Please cite this article in press as: Kananian et al., A disposable reader-sensor solution for wireless temperature logging, Device (2023), https://doi.org/10.1016/j.device.2023.100183





$$\begin{bmatrix} I_{L1} \\ I_{L2} \end{bmatrix} + \begin{bmatrix} j\omega C_1 & 0 \\ 0 & j\omega C_2 + G_S \end{bmatrix} \begin{bmatrix} V_1 \\ V_2 \end{bmatrix} + \begin{bmatrix} I_1 \\ 0 \end{bmatrix} = 0 \qquad \text{(Equation 6)}$$

where $G_S = \frac{1}{R_S}$ and $i(t) = \text{Re}\,[I_1 e^{j\omega t}]$. Substituting Equation 5 into Equation 6 yields

$$\begin{bmatrix} -I_1 \\ 0 \end{bmatrix} = \begin{bmatrix} j\omega C_1 + \frac{1}{j\omega L_1(1-\kappa^2)} & -\frac{\kappa}{j\omega\sqrt{L_1 L_2}(1-\kappa^2)} \\ -\frac{\kappa}{j\omega\sqrt{L_1 L_2}(1-\kappa^2)} & G_S + j\omega C_2 + \frac{1}{j\omega L_2(1-\kappa^2)} \end{bmatrix} \begin{bmatrix} V_1 \\ V_2 \end{bmatrix}. \qquad \text{(Equation 7)}$$

Solving Equation 7 yields the equivalent admittance of the sensor resonator as seen from the reader resonator, $Y^{\text{coupled}}(\omega) = -\frac{I_1}{V_1}$, which is given by

$$Y^{\text{coupled}}(\omega) = j\omega C_1 + \frac{1}{j\omega \widehat{L}_1} + \frac{\frac{\kappa^2}{\omega^2 \widehat{L}_1 \widehat{L}_2}}{G_S^2 + \left(\omega C_2 - \frac{1}{\omega \widehat{L}_2}\right)^2} \left(G_S - j\omega C_2 - \frac{1}{j\omega \widehat{L}_2}\right) \qquad \text{(Equation 8)}$$

where $\widehat{L}_n = (1-\kappa^2)L_n$ for $n = 1, 2$. Separating the real and the imaginary parts, we obtain

$$G^{\text{coupled}}(\omega) = \frac{\frac{\kappa^2}{\omega^2 \widehat{L}_1 \widehat{L}_2}}{G_S^2 + \left(\omega C_2 - \frac{1}{\omega \widehat{L}_2}\right)^2} G_S \qquad \text{(Equation 9)}$$

$$B^{\text{coupled}}(\omega) = \left(\omega C_1 - \frac{1}{\omega \widehat{L}_1}\right) \left[1 - \frac{\frac{\kappa^2}{\omega^2 \widehat{L}_1 \widehat{L}_2}}{G_S^2 + \left(\omega C_2 - \frac{1}{\omega \widehat{L}_2}\right)^2} \frac{\omega C_2 - \frac{1}{\omega \widehat{L}_2}}{\omega C_1 - \frac{1}{\omega \widehat{L}_1}}\right]. \qquad \text{(Equation 10)}$$

Roots of $B^{\text{coupled}}(\omega) = 0$ correspond to the self-oscillating modes. When $L_1 = L_2$ and $C_1 = C_2$, there are 6 roots and 3 possible self-oscillating modes. Two of the three modes are stable in the strongly coupled region and satisfy

$$\frac{\frac{\kappa^2}{\omega^2 \widehat{L}_1 \widehat{L}_2}}{G_S^2 + \left(\omega C_2 - \frac{1}{\omega \widehat{L}_2}\right)^2} = 1. \qquad \text{(Equation 11)}$$

Hence, $B^{\text{coupled}}(\omega) = G_S$. Around the eigenfrequency of each stable mode, we could approximate the susceptance by an LC tank.

## Circuit simulation

The cross-coupled CMOS pair was simulated using the circuit simulator from Cadence based on parameters listed in Table S1. To obtain the I-V curve, the differential voltage, $v$, applied to the gates of the transistors was swept, and the current $i$ delivered to the LC tank by the cross-coupled CMOS pair was measured using a current probe. To characterize the relationship between the amplitude of oscillation and sensor resistance, we performed a time-domain simulation. For each resistance value, we started the simulation with a small initial value (10 mV), waited until steady state is reached, and recorded the amplitude of oscillation. To characterize the locking capability, the reader circuit was coupled to a sensor resonator with the same $L$ and $C$ as the reader resonator.

## Design of the custom reader chip and hybrid resonator

The custom reader chip implements a CMOS cross-coupled pair, an envelope detector, a high-frequency audio transmitter, a power management unit, and part of the reader resonator. The CMOS cross-coupled pair is detailed in Figure 3A and Table S1. It is reset before each amplitude locking to prevent hysteresis. It is alternating-current-coupled (ac-coupled) to the envelope detector. The envelope detector is implemented using a source-follower stage with PMOS transistors in weak inversion ($g_m/I_d$ = 24.9). PMOS transistors are used to eliminate body effect. Output from the envelope detector is first converted to a proportional current using a voltage-controlled current source (VCCS). The VCCS consists of an operational transconductance amplifier (OTA) and a PMOS current mirror. The bias current of the OTA comes from the power management unit (PMU). The overall transconductance of the VCCS is determined by a 3-bit resistive digital-to-analog converter (RDAC), which can be programmed between 2.5 MΩ and 6 MΩ with steps of around 560 kΩ. The generated current is then used to tune the frequency of a ring oscillator. The output frequency of the ring oscillator $f_0$ is in the range of 100 kHz to 1 MHz. A divider is used to scale the frequency to the range of 16–20 kHz ($f_{TX}$), which then drives a piezoelectric thin film.

For the reader resonant circuit, the value of the inductor is 0.73 μH, and the nominal value for the capacitor is 39 pF. The inductor is implemented off chip due to on-chip quality factor (Q-factor) degradation. It is in a planar circular structure and fabricated on a flexible substrate. The outside diameter of the inductor is 2.5 cm with 5 turns and trace width of 0.7 mm, and the spacing between turns is 0.2 mm. The Q-factor is about 170 in the frequency range of 25–38 MHz. For the capacitor, due to area constraints, part of it is implemented on chip, and part of it is off chip. The on-chip capacitor is implemented as a capacitor array with a maximum value of 25.6 pF, and the off-chip capacitor is fixed at 20 pF. The on-chip capacitor array is programmable with a step size of 0.4 pF to accommodate different sensing applications. The programmability of the capacitor array is also utilized to compensate for the finite Q-factor of the off-chip inductor. The sensing error is ~1% without compensation[33] and is reduced to ~0.1% with compensation.[25] Unlike conventional schemes based on measuring resonant frequency shifts at the sensor, where active tuning is indispensable, active tuning is optional for the sensing scheme presented in this work, and the improvement is small.

The custom reader chip was designed using 40-nm CMOS technology from Taiwan Semiconductor Manufacturing. Simulations were performed using Cadence, and digital circuits were developed in Verilog and synthesized using IC Compiler from Synopsys. The reader coil in the resonant circuit was first designed based on a mathematical model and then optimized using the full-wave electromagnetic simulator in Ansys HFSS.

## Design of the wireless power link

We used a wirelessly powered light-emitting diode-based (LED-based) NFC tag from Adafruit to locate the NFC antenna on an iPhone. Several coils were manufactured on flexible PCB and were characterized to determine the highest attainable Q. However, we found out that there was no major difference in Q-factor among various designs. Our coil dimension is 3 cm by 1 cm with 6 turns, in which both spacing between turns and trace width equal 0.3 mm. There is no impedance matching at the interface of the antenna and rectifier. The inductance of the antenna is canceled using a parallel capacitor resonating at 13.56 MHz. Because power levels harvested from the NFC signal are much larger than the power level of the silicon chip, an off-chip, one-stage rectifier is used. A Zener diode (Z) is used to limit the harvested voltage to 3.3 V, which is the maximum voltage that thick-oxide transistors in the used CMOS technology can support. As a result, the rectifier generates an unregulated 3.3-V supply to power the custom reader integrated circuit.

During the NFC polling mode, when the rectifier output reaches 3.3 V, the on-chip PMU turns on. The PMU consists of a band-gap reference circuit that generates a 0.8-V supply. This reference supply is then used to generate two voltage levels using two programmable low drop-out regulators: a 3-V supply for analog blocks and a 1.1-V supply for digital blocks.

## Characterization of the wireless reader-sensor link

A resonator that is identical to the reader resonator is connected in parallel with a potentiometer to form the passive sensor. The potentiometer is swept over the resistance range. While varying the resistance ($R_S$), the distance between the sensor and the reader is varied in steps of 0.2 cm. Output from the audio transmitter is recorded by the same smartphone that is used to power the

reader. We use Phyphox, an app developed at RWTH Aachen University to access the microphone and record the audio signal. Fast Fourier Transform (FFT) is performed offline on the recorded signal to derive the frequency of the audio signal, which corresponds to the frequency-modulated envelope locked by the self-running oscillator.

### Simulation of the inverted U-shaped gallium structure

We performed fluid dynamics simulations to investigate the effect of surface tension forces in the deformation of the gallium structure. By assuming the structure to be fully melted and in liquid form, we used an in-house, two-phase flow solver based on a second-order conservative phase field method[34,35] to study the evolution of the two-phase system comprising liquid gallium and gaseous air. We used realistic material properties at 32°C with a liquid density of $\rho_l = 6095 kg/m^3$, liquid viscosity of $\mu_l = 1.99 \times 10^{-3}$ kg/m/s, gas density of $\rho_g = 1.2 kg/m^3$, gas viscosity of $\mu_g = 1.81 \times 10^{-5}$ kg/m/s, and surface tension of $\sigma = 0.71 N/m$. Due to the short timescale of the problem, we ignored the effect of gravity. The initial conditions of the simulation were given by a quiescent system, using the geometry in Figure S2, lying on a solid wall. The domain size was 12 × 12 × 1.5 $mm^3$ with a uniform mesh of 256 × 256 × 32 cells. For velocity, no slip boundary conditions were enforced on the wall on which the structure lies, and free slip boundary conditions were used on all other boundaries. For the volume fraction variable, Neumann boundary conditions were used on all boundaries, including the solid wall, resulting in 90° static contact angles. The evolution of the fluid system due to the interaction of surface tension forces, viscous forces, and inertia can be observed in Figure 5B. It is clear that surface tension forces first act to smoothen sharp edges of the structure. As the surface tension continues to drive the system toward a state of energy minimization by reducing the surface area of the gallium-air interface, the structure loses contact with the carbon electrodes, and an open circuit configuration is reached. This agrees with our experimental observations.

In the simulation, the surface reduction due to capillary flows continues for this two-phase flow, where the gallium structure evolves toward a hemispherical drop after a very long time. In experiments, however, a 1-nm solid oxide layer forms at much shorter timescales at the interface between liquid and gas. This oxide layer essentially resists stretching but allows compression or wrinkling of the interface. Therefore, in the initial stage of the process, surface tension can deform the structure with no resistance from the oxide layer because the majority of surface deformations are locally reducing the surface area (compressing or wrinkling the oxide layer). However, at longer times, further deformations of the structure predicted by fluid simulations are prevented because they would require local stretching of the interface. In summary, the fluid simulations were predictive of the early stage of deformation and explain how the open circuit is attained. The slowdown of deformations that was observed in the experiments was nevertheless not observed in fluid simulations but rather explained phenomenologically by restriction to stretching of the interface imposed by the solid oxide layer.

### Fabrication of the binary irreversible temperature sensor

Carbon electrodes positioned underneath the gallium structure act as a stable connection between gold pads and gallium, preventing spontaneous alloy formation at the gold-gallium interface.[36] Both gold and carbon electrodes were fabricated using the conventional semiconductor dry process. The sensor was fabricated on a 4-in Pyrex 7740 glass wafer rather than a silicon wafer to mitigate substrate conduction. A 1-μm positive photoresist (PR) layer (SPR 3612) was used and patterned with 405 nm (MLA150 Maskless Aligner, Heidelberg Instruments, Heidelberg, Germany). Over the patterned PR, 150 Å of titanium for the adhesion layer and 2,000 Å of gold for contact electrodes were evaporated sequentially and lifted off. Carbon electrodes were fabricated by a repeated dripping and drying process (drop casting) of 0.5 mg/mL of CNT solution dissolved in 50% ethanol until each sensor array reached a resistance of 100 ω. Carbon electrodes were patterned with PR and etched with $O_2$ plasma with 20 sccm, 15 Pa, and radio-frequency (RF) power of 100 W for 3 min. After removing the PR pattern used to protect the carbon electrode from etching, the carbon electrode on the gold pattern was stored under dry condition. The size of the final electrodes was 4 mm in width and 2 mm in height for gold electrodes and 2.4 mm in width and 2 mm in height for carbon electrodes.

The gallium mold was fabricated by conventional soft lithography using PDMS. A 4-in silicon wafer was cleaned with acetone, methanol, and deionized (DI) water sequentially. Three negative PR layers (SU-8 2050) were coated by spin coating (500 rpm for 10 s followed by 1,500 rpm for 30 s), and consecutive soft baking was performed (65°C for 5 min, 90°C for 25 min), which was patterned with an I-line contact aligner (Karl Süss MA-6, SÜSS MicroTec, Garching, Germany) with an intensity of 15 $mW/cm^2$ for 12 s to fabricate a master mold. The pattern was developed with an SU-8 developer for 15 min and then rinsed with isopropyl alcohol and DI water. The developed pattern had a thickness of 340 μm, which was verified by ellipsometry characterization. The SU-8 master mold was placed in a Petri dish 120 mm in diameter, where PDMS was poured and cured at 60°C for 3 h. The PDMS mold was cut, punched by a hole punch cutter (1-mm diameter) at the inlet and outlet of the pattern, and placed on the carbon electrodes. A piece of gallium (99.99% trace metals basis, Millipore Sigma, Burlington, MA, USA) was placed in a centrifugal tube in warm water (~60°C for 5 min) to be completely melted. The liquid form of gallium was injected into the inlet of the PDMS pattern with a syringe needle. The syringe and needle were warmed up in warm water (60°C) and dried right before the experiment, and the PDMS pattern on the Pyrex glass wafer was placed onto the hot plate (60°C) for the entire process to prevent solidification of the gallium during the injection. Vacuum was applied to the outlet of the PDMS pattern in case the injection was incomplete. The entire structure with the electrodes, gallium, and mold was stored in a refrigerator (4°C) until it solidified. Then the mold was carefully removed from the substrate to produce a free-standing gallium structure.

### Characterization of the wireless temperature sensor

A binary irreversible temperature sensor was connected in parallel to an inductor (0.73 μH) and a capacitor (39 pF) using conductive tape. The sensor was placed on a heat source (THMS600, Linkam, Surrey, UK). The resistance and resonant frequency of the sensor were measured by a network analyzer (E5072A, Agilent Technologies, CA, USA) every 2 s at different temperatures higher than the melting point of gallium (Figure S4). During gallium deformation, not only does the resistance change, but the resonant frequency also changes (Figure S5). This can be attributed to the change in the physical shape and volume of the gallium structure, resulting in a change in capacitance. However, at steady state, differences in the resonant frequency between the high-impedance and the low-impedance states are relatively small. The on-chip capacitor array in the reader circuit can be utilized to accommodate this variation.

### Characterization of the wireless link between the reader and the temperature sensor

To validate the wireless reader-sensor link, a standalone wireless temperature sensor was placed on a heat source (THMS600, Linkam) at 32°C for 160 s (the average switching time of the gallium structure at 32°C is about 122 s) Sensor resistance measurements were sent to the phone via the audio transmitter in the reader chip. We used the app Phyphox, to access the microphone and record the audio signal and another app, Pythonista 3, to perform real-time post-processing (taking the fast Fourier transform) on the phone. The state of the sensor was then displayed on the phone screen.

### Measurement setup for wireless tracking of temperature-sensitive food

The temperature sensor was attached to the inside of a box of chocolate truffles. The box was stored in a refrigerator. To simulate room temperature on a hot day, the box of chocolate truffles was placed in an oven (Blue M, TPS, PA, USA) set to 31°C for 20 min. Then, the box was stored back in the refrigerator. During the experiment, the states of the sensor were measured from the outside of the box with the sticker-like reader attached to a smartphone. As shown in Video S3, the temperature was raised to 35°C for 20 min, and therefore, the sensor changed state in less than 10 min of heat exposure.

## SUPPLEMENTAL INFORMATION

Supplemental information can be found online at https://doi.org/10.1016/j.device.2023.100183.

## ACKNOWLEDGMENTS

The authors thank the Taiwan Semiconductor Manufacturing Company for chip fabrication. The authors would like to thank Dr. Mazhareddin Taghivand and Dr. Kamal Aggarwal for insightful discussions. This work was supported by a Qualcomm Innovation Fellowship and the Chan Zuckerberg Biohub.

## AUTHOR CONTRIBUTIONS

S.K. and A.S.Y.P. conceived the idea of the self-oscillating reader. J.R. and A.S.Y.P. conceived the idea of the irreversible temperature sensor. S.K. and A.S.Y.P. contributed to formulating the analytical model for the self-oscillating reader. S.K. and C.C. designed the reader silicon chip and performed the chip characterization. S.K. developed the entire reader circuitry and the sensor circuitry. J.R. designed and fabricated the sensor. J.R. and A.D. characterized the sensor. S.K. and J.R. conducted experiments and analyzed the data. S.N., A.D., and M.-g.K. contributed to discussions about sensor fabrication. S.M. and A.M. performed simulation of the gallium structure. H.-S.P.W., Z.B., and E.P. provided personnel. S.K., J.R., and A.S.Y.P. wrote the manuscript. All authors read and discussed the manuscript.

## DECLARATION OF INTERESTS

S.K. and A.S.Y.P. are co-inventors of a patent covering the design of the reader, filed by Stanford.

## DECLARATION OF GENERATIVE AI AND AI-ASSISTED TECHNOLOGIES IN THE WRITING PROCESS

During the preparation of this work, the authors used ChatGPT to check for grammatical errors in the writing. After using this tool, the authors reviewed and edited the content as needed and take full responsibility for the content of the publication.

Received: August 29, 2023
Revised: October 30, 2023
Accepted: November 6, 2023
Published: December 1, 2023

## REFERENCES

1. Galliani, D., Mascheroni, L., Sassi, M., Turrisi, R., Lorenzi, R., Scaccabarozzi, A., Stingelin, N., and Beverina, L. (2015). Thermochromic Latent-Pigment-Based Time-Temperature Indicators for Perishable Goods. Adv. Opt. Mater. *3*, 1164–1168.
2. Heywood, J.T., Jermyn, R., Shavelle, D., Abraham, W.T., Bhimaraj, A., Bhatt, K., Sheikh, F., Eichorn, E., Lamba, S., Bharmi, R., et al. (2017). Impact of Practice-Based Management of Pulmonary Artery Pressures in 2000 Patients Implanted With the CardioMEMS Sensor. Circulation *135*, 1509–1517.
3. Jeon, J., Lee, H.-B.-R., and Bao, Z. (2013). Flexible Wireless Temperature Sensors Based on Ni Microparticle-Filled Binary Polymer Composites. Adv. Mater. *25*, 850–855.
4. Wu, S.-Y., Yang, C., Hsu, W., and Lin, L. (2015). 3D-printed microelectronics for integrated circuitry and passive wireless sensors. Microsyst. Nanoeng. *1*, 15013.
5. Waimin, J., Gopalakrishnan, S., Heredia-Rivera, U., Kerr, N.A., Nejati, S., Gallina, N.L.F., Bhunia, A.K., and Rahimi, R. (2022). Low-Cost Nonreversible Electronic-Free Wireless pH Sensor for Spoilage Detection in Packaged Meat Products. ACS Appl. Mater. Interfaces *14*, 45752–45764.
6. Pasupathy, P., Trivedi, T., Leonhardt, B., Zhang, S., Ekerdt, J.G., and Neikirk, D.P. (2017). Miniature Passive Wireless Resonant Platform for Chemical Memory-Based Threshold Sensing. IEEE Sensor. J. *17*, 1209–1210.
7. Boutry, C.M., Beker, L., Kaizawa, Y., Vassos, C., Tran, H., Hinckley, A.C., Pfattner, R., Niu, S., Li, J., Claverie, J., et al. (2019). Biodegradable and flexible arterial-pulse sensor for the wireless monitoring of blood flow. Nat. Biomed. Eng. *3*, 47–57.
8. Lu, D., Yan, Y., Avila, R., Kandela, I., Stepien, I., Seo, M.H., Bai, W., Yang, Q., Li, C., Haney, C.R., et al. (2020). Bioresorbable, Wireless, Passive Sensors as Temporary Implants for Monitoring Regional Body Temperature. Adv. Healthcare Mater. *9*, 2000942.
9. Carr, A.R., Patel, Y.H., Neff, C.R., Charkhabi, S., Kallmyer, N.E., Angus, H.F., and Reuel, N.F. (2020). Sweat monitoring beneath garments using passive, wireless resonant sensors interfaced with laser-ablated microfluidics. NPJ Digit. Med. *3*, 62.
10. Lee, J., Ihle, S.J., Pellegrino, G.S., Kim, H., Yea, J., Jeon, C.-Y., Son, H.-C., Jin, C., Eberli, D., Schmid, F., et al. (2021). Stretchable and suturable fibre sensors for wireless monitoring of connective tissue strain. Nat. Electron. *4*, 291–301.
11. Yang, M.X., Hu, X., Akin, D., Poon, A., and Wong, H.-S.P. (2021). Intracellular detection and communication of a wireless chip in cell. Sci. Rep. *11*, 5967.
12. Chen, L.Y., Tee, B.C.-K., Chortos, A.L., Schwartz, G., Tse, V., Lipomi, D.J., Wong, H.-S.P., McConnell, M.V., and Bao, Z. (2014). Continuous wireless pressure monitoring and mapping with ultra-small passive sensors for health monitoring and critical care. Nat. Commun. *5*, 5028.
13. Tan, E.L., Ng, W.N., Shao, R., Pereles, B.D., and Ong, K.G. (2007). A Wireless, Passive Sensor for Quantifying Packaged Food Quality. Sensors *7*, 1747–1756.
14. Kondalkar, V.V., Li, X., Park, I., Yang, S.S., and Lee, K. (2018). Development of chipless, wireless current sensor system based on giant magneto-impedance magnetic sensor and surface acoustic wave transponder. Sci. Rep. *8*, 2401.
15. Chen, P.-Y., Sakhdari, M., Hajizadegan, M., Cui, Q., Cheng, M.M.-C., El-Ganainy, R., and Alù, A. (2018). Generalized parity–time symmetry condition for enhanced sensor telemetry. Nat. Electron. *1*, 297–304.
16. Sakhdari, M., Hajizadegan, M., Li, Y., Cheng, M.M.-C., Hung, J.C.H., and Chen, P.-Y. (2018). Ultrasensitive, Parity–Time-Symmetric Wireless Reactive and Resistive Sensors. IEEE Sensor. J. *18*, 9548–9555.
17. Collins, C.C. (1967). Miniature Passive Pressure Transensor for Implanting in the Eye. IEEE Trans Biomed Eng *BME*-. IEEE Trans. Biomed. Eng. *14*, 74–83.
18. Dong, Z., Li, Z., Yang, F., Qiu, C.-W., and Ho, J.S. (2019). Sensitive readout of implantable microsensors using a wireless system locked to an exceptional point. Nat. Electron. *2*, 335–342.
19. Nopper, R., Has, R., and Reindl, L. (2011). A Wireless Sensor Readout System—Circuit Concept, Simulation, and Accuracy. IEEE Trans. Instrum. Meas. *60*, 2976–2983.
20. Kananian, S., Alexopoulos, G., and Poon, A.S. (2020). Coupling-Independent Real-Time Wireless Resistive Sensing Through Nonlinear PT Symmetry. Phys. Rev. Appl. *14*, 064072.
21. Donaldson, P.E. (1987). Power for neurological prostheses: A simple inductive R.F. link with improved performance. J. Biomed. Eng. *9*, 194–197.
22. Assawaworrarit, S., Yu, X., and Fan, S. (2017). Robust wireless power transfer using a nonlinear parity–time-symmetric circuit. Nature *546*, 387–390.
23. Strogatz, S.H. (2000). Nonlinear Dynamics and Chaos: With Applications to Physics, Biology, Chemistry, and Engineering (Studies in Nonlinearity) (CRC Press).
24. Gray, Paul R., Hurst, Paul J., Lewis, Stephen H., and Meyer, Robert G. (2009). Analysis and Design of Analog Integrated Circuits (Wiley).
25. Kananian, S., Chen, C., and Poon, A.S.Y. (2022). An energy-harvesting stamp-sized reader for distance-immune interrogation of passive wireless sensors. In Proceedings of the Custom Integrated Circuits Conference (Institute of Electrical and Electronics Engineers Inc.).
26. Ashihara, K. (2007). Hearing thresholds for pure tones above 16kHz. J. Acoust. Soc. Am. *122*, EL52–EL57.

Please cite this article in press as: Kananian et al., A disposable reader-sensor solution for wireless temperature logging, Device (2023), https://doi.org/10.1016/j.device.2023.100183



27. Xu, Z., Li, X., Zhu, Z., Wang, Q., Chen, Y., and Ma, T. (2020). Experimental study on the heat transfer performance of a gallium heat sink. Energy Convers. Manag. *213*, 112853.

28. Wang, H., Chen, S., Zhu, X., Yuan, B., Sun, X., Zhang, J., Yang, X., Wei, Y., and Liu, J. (2022). Phase transition science and engineering of gallium-based liquid metal. Matter *5*, 2054–2085.

29. Scharmann, F., Cherkashinin, G., Breternitz, V., Knedlik, C., Hartung, G., Weber, T., and Schaefer, J.A. (2004). Viscosity effect on GaInSn studied by XPS. In Surface and Interface Analysis, pp. 981–985.

30. Tulliani, J.M., Inserra, B., and Ziegler, D. (2019). Carbon-based materials for humidity sensing: A short review. Micromachines *10*, 232.

31. Zhou, J., Zhou, T., and Xu, P. (2021). Calculation of flow heat transfer characteristics of liquid gallium. International Journal of Advanced Nuclear Reactor Design and Technology *3*, 175–183.

32. Ma, K., and Liu, J. (2007). Liquid metal cooling in thermal management of computer chips. Front. Energy Power Eng. China *1*, 384–402.

33. Kananian, S., Alexopoulos, G., and Poon, A.S.Y. (2022). Robust Wireless Interrogation of Fully-Passive RLC Sensors. IEEE Trans. Circ. Syst. I. *69*, 1427–1440.

34. Mirjalili, S., and Mani, A. (2021). Consistent, energy-conserving momentum transport for simulations of two-phase flows using the phase field equations. J. Comput. Phys. *426*, 109918.

35. Mirjalili, S., Ivey, C.B., and Mani, A. (2020). A conservative diffuse interface method for two-phase flows with provable boundedness properties. J. Comput. Phys. *401*, 109006.

36. Cooke, C.J., and Hume-Rothery, W. (1966). The equilibrium diagram of the system gold-gallium. Journal of the Less Common Metals *10*, 42–51.